Research Article Vol. 30, No. 17 / 15 Aug 2022 / Optics Express 30135
Optics EXPRESS

Fingerprint multiplex CARS at high speed based on supercontinuum generation in bulk media and deep learning spectral denoising

FEDERICO VERNUCCIO,[1] ARIANNA BRESCI,[1] BENEDETTA TALONE,[1] ALEJANDRO DE LA CADENA,[1] CHIARA CECONELLO,[1] STEFANO MANTERO,[2,3] CRISTINA SOBACCHI,[2,3] RENZO VANNA,[4] GIULIO CERULLO,[1,4] AND DARIO POLLI[1,4,*]

[1]*Department of Physics, Politecnico di Milano, P.zza Leonardo da Vinci 32, 20133 Milan, Italy*
[2]*CNR-Institute for Genetic and Biomedical Research (CNR-IRGB), via Fantoli 16/15, 20138 Milan, Italy*
[3]*IRCCS Humanitas Research Hospital, via Manzoni 56, 20089 Rozzano (Mi), Italy*
[4]*CNR-Institute for Photonics and Nanotechnologies (IFN-CNR), P.zza Leonardo Da Vinci 32, 20133 Milan, Italy*
[*]*dario.polli@polimi.it*

Abstract: We introduce a broadband coherent anti-Stokes Raman scattering (CARS) microscope based on a 2-MHz repetition rate ytterbium laser generating 1035-nm high-energy (≈μJ level) femtosecond pulses. These features of the driving laser allow producing broadband red-shifted Stokes pulses, covering the whole fingerprint region (400–1800 cm^{-1}), employing supercontinuum generation in a bulk crystal. Our system reaches state-of-the-art acquisition speed (<1 ms/pixel) and unprecedented sensitivity of ≈14.1 mmol/L when detecting dimethyl sulfoxide in water. To further improve the performance of the system and to enhance the signal-to-noise ratio of the CARS spectra, we designed a convolutional neural network for spectral denoising, coupled with a post-processing pipeline to distinguish different chemical species of biological tissues.

1. Introduction

Every molecular component of a biological specimen features a unique vibrational spectrum carrying a chemical information that can be exploited as a fingerprint for its identification. Vibrational microscopy is a powerful technique to image cells and tissues [1,2] in a label-free and non-invasive manner. Spontaneous Raman (SR) is one of the most widespread vibrational microscopy techniques and it is particularly adequate for high spectral resolution imaging of biological and water-containing samples [3,4]. In SR the specimen is illuminated with quasi-monochromatic visible or near-infrared (NIR) laser light at the pump frequency ω_p. The vibrational information is encoded in the spontaneously emitted inelastically scattered Stokes and anti-Stokes spectra, at frequencies $\omega_s=\omega_p-\Omega$ and $\omega_{aS}=\omega_p+\Omega$, respectively, where the frequency shift Ω is a vibrational mode of the sample. Because the probed molecules follow a Boltzmann distribution, i.e., the molecules mostly remain in their lowest energy levels at thermal equilibrium, the Stokes component is more intense than the anti-Stokes component. Therefore, conventional Raman scattering systems detect Stokes scattering. SR provides the maximum amount of vibrational information; however, it suffers from very low scattering cross-sections, requiring long acquisition times of the order of ≈ 1 s per pixel, preventing high-speed imaging.

Coherent Raman scattering (CRS) [5,6] exploits a third-order non-linear interaction between the sample and the impinging electric fields that coherently excite the molecular vibrations in the focal volume, thus enhancing the signal by several orders of magnitudes with respect to SR and inherently providing three-dimensional sectioning capability without the need of any

#463032 https://doi.org/10.1364/OE.463032
Journal © 2022 Received 6 May 2022; revised 14 Jul 2022; accepted 14 Jul 2022; published 2 Aug 2022

Optics EXPRESS

confocal aperture. In its simplest configuration, CRS employs two narrowband picosecond pulses at frequency ω_p (the pump) and ω_s (the Stokes), such that their difference $\Omega = \omega_p$-ω_s matches a vibrational mode of the scrutinized sample. In this case, a single vibrational mode can be probed at a time, limiting the amount of chemical information that can be acquired. Broadband CRS [7] aims at combining the high acquisition speed of single-frequency CRS with the detailed chemical information delivered by SR.

The two most-commonly employed CRS techniques are stimulated Raman scattering (SRS) [8] and coherent anti-Stokes Raman scattering (CARS) [9,10]. SRS measures the intensity gain of the Stokes beam (stimulated Raman gain) or the intensity loss of the pump beam (stimulated Raman loss), while CARS detects the background-free signal at the anti-Stokes frequency $\omega_{as} = \omega_p + \Omega$. Because it is proportional to the absorptive imaginary part of the third-order susceptibility $\chi^{(3)}$, the SRS signal delivers spectral line shapes that are almost identical to the Lorentzian peaks obtained with SR and scales linearly with the concentration of scatterers. However, since SRS is a small signal sitting on top of the intense pump and Stokes beams, sophisticated high-frequency modulation transfer techniques are necessary for its detection, making the SRS approach technically complex, especially for broadband implementations [11,12]. Instead, in the CARS technique, the signal is blue shifted with respect to the pump/Stokes pulses. Thus, after filtering out the pump-Stokes radiation, a simple spectrometer can effectively detect the anti-Stokes component, significantly reducing the technical complexity of the system. On the downside, the CARS signal is proportional to the square of the concentration of scatterers and suffers from the presence of a chemically unspecific contribution, which is known as non-resonant background (NRB), due to a four-wave-mixing process mediated by the non-resonant $\chi^{(3)}$ of the sample. Although the NRB distorts and in some cases overwhelms the vibrational line shapes, limiting the sensitivity of the CARS apparatus, it can also act as a phase-coherent local oscillator, allowing heterodyne amplification of the weak resonant Raman response [13]. While in a narrowband configuration such amplification is of little help, in broadband CARS (B-CARS) the NRB can be exploited to increase the signal-to-noise ratio (SNR) [14] and the line shape distortions can be removed exploiting numerical methods [15–17] or deep-learning approaches [18–20].

Despite many improvements in the detection systems, leading to higher speed and broader spectral coverage, many B-CARS systems are designed to collect Raman spectra only in the CH-stretching region [21] (2800 - 3100 cm^{-1}), a spectral range that features a high density of oscillators. Spectral information in this region is rather unspecific, preventing accurate identification within chemically heterogenous biological samples. On the contrary, the low-wavenumber spectral region (400–1800cm^{-1}), also known as "fingerprint", presents sharp and distinct peaks providing high biochemical specificity. However, the fingerprint region features weaker Raman signals requiring either longer integration times or higher average power of the pump and Stokes beams to obtain sufficiently high SNR. These requirements could lead to damage of the imaged biological samples. Moreover, the Raman peaks in the fingerprint region present narrow linewidths and are spectrally congested, demanding a combination of high spectral resolution (down to 10 cm^{-1}) and broad spectral coverage, which are technically challenging to achieve.

Several B-CARS microscopy setups covering the fingerprint region have been reported in the literature. Some of them exploit the rapid frequency tuning of one of the two narrowband beams (the so-called hyperspectral CARS method [22]), while other approaches, known as multiplex CARS [14,23–26], aim at measuring the complete spectrum in parallel, covering both the fingerprint and the CH-stretching regions. Multiplex CARS employs either a single ultra-broadband laser providing both pump and Stokes frequencies [27,28] or the combination of a narrowband pump with a broadband Stokes obtained by supercontinuum generation in a tapered fiber [29] or a photonic crystal fiber (PCF) [30,31]. Some approaches are based on a time-domain

Optics EXPRESS

Fourier transform approach [32–34] or use frequency combs [35], while others detect the CARS signal in the frequency domain. Hashimoto *et al.* [33] reported broadband (spectral coverage: 200–1500 cm^{-1}) CARS spectroscopy at a record scan rate of 24,000 spectra/s using a time-domain Fourier-transform approach, while Camp *et al.* [14] presented ultrabroadband (spectral coverage: 500–3500 cm^{-1}) multiplex CARS microspectroscopy at 3.5-ms pixel exposure time. Yoneyama *et al*. [26] developed a multiplex CARS microscope (spectral coverage: 600–3600 cm^{-1}) with exposure time down to 0.8 ms, using a high-peak-power supercontinuum generated in a PCF pumped by a Q-switched microchip Nd: YVO_4 laser oscillator generating sub-100-ps laser pulses at 0.82-MHz repetition rate.

The low B-CARS signal levels in the fingerprint region have led to the use of post-processing methods to enhance the SNR while preserving the chemical information contained in the collected hyperspectral images. Several numerical methods have been used to denoise B-CARS images, which are 3D data hypercubes characterized by two spatial and one spectral dimension, such as principal component analysis or singular value decomposition [14] and spectral total variation [36]. Recently, deep-learning methods [37] based on convolutional neural networks (CNN) have been used for broadband CRS images affected by Gaussian noise. These are supervised methods in which the neural model is trained with pairs consisting of a noisy input and an ideal output, finding the best nonlinear transfer function that transforms the former into the latter. The trained model is then tested on previously unseen experimental data. The first demonstration of CRS image denoising through CNN architectures was performed by Manifold et al. [38], who employed a U-net CNN [39] architecture for SRS signals. CNNs for denoising CARS endoscopic images have been later applied by Yamato et al. [40]. Finally, Lin et al. [41] developed a spatial-spectral residual net, based on the U-net architecture, to denoise hyperspectral SRS images, training the model on images containing similar spatial features as those to be denoised.

Here we demonstrate a novel approach to B-CARS based on an amplified femtosecond ytterbium laser system working at 2-MHz repetition rate, that delivers pulses at 1035 nm with much higher (≈J level) energy than standard systems typically running at 40 or 80 MHz. This unlocks two key advantages. The first is the possibility to generate broadband red-shifted Stokes pulses, covering the whole fingerprint region (400–1800cm^{-1}), employing white-light continuum (WLC) generation [42] in a bulk crystal rather than in PCFs, as previously reported in literature. WLC in bulk media is a more compact, robust, simple and alignment-insensitive technique. It exhibits high mutual correlations between the intensities of its spectral components, low pulse-to-pulse fluctuations, and excellent long-term stability, which is comparable to that of the pump laser source itself [43]. The second advantage relates to the reduced repetition rate. On the one hand, a repetition rate of 2 MHz allows a temporal delay of 0.5 µs between two consecutive pulses, leaving more time to the system for thermal energy dissipation, thus reducing photothermal damage [44]. On the other hand, for a given average power at the focus, limited by sample degradation, higher pulse energy results in higher peak intensity, which generates a stronger B-CARS signal thanks to the non-linear nature of the optical effect. This entails higher SNR and/or acquisition speed, without compromising sample integrity.

Our B-CARS microscope delivers high-quality images at state-of-the-art acquisition speed, with <1 ms pixel dwell time for polymer beads, limited by the spectrometer refresh rate. It also features enhanced chemical specificity and sensitivity to low concentrations. The performance of our microscope is boosted by two further crucial characteristics. On the one hand, our setup, working in a red-shifted spectral region (1035 nm for the pump and 1050 - 1300 nm for the Stokes beam) with respect to standard CARS setups (800 nm for the pump, 830 - 1000 nm for the Stokes), enables us to employ higher laser intensities on the sample before the onset of photo-damage [45], thanks to a reduced multi-photon absorption from cell/tissue pigments and especially DNA, which absorbs around 260 nm. On the other hand, we employ an innovative data processing pipeline that extracts the maximum amount of information from the recorded

Optics EXPRESS

B-CARS hypercubes. Our data-processing pipeline includes: (i) a spectral denoiser based on a CNN architecture that increases the SNR of the acquired B-CARS spectra; (ii) a numerical method to remove NRB from the spectra, based on the Kramers-Kronig relations [17]; and (iii) a multivariate curve resolution-alternating least squares (MCR-ALS) algorithm [46] and a K-means cluster analysis (KMCA) algorithm [47] to discern the different chemical constituents. In this paper we demonstrate very fast vibrational hyperspectral imaging with high SNR on solvents and polymer beads, and we validate the potential of our approach for biomedical imaging by mapping murine spine longitudinal sections.

2. Methods

The architecture of the B-CARS microscope is shown in Fig. 1 and described in detail in the supplemental document. A commercial fiber-based ytterbium laser system provides ≈270 fs pulses at 1035 nm wavelength with variable repetition rate and average power, which we fixed at 2 MHz and ≈5W, respectively. A polarizing beam splitter divides the laser output into two beams, whose average powers are controlled by a half-wave plate mounted on a manual rotational stage. The first fraction of the beam, with ≈2-W average power, generates narrowband pump pulses with energy fluctuations <1% RMS by spectral filtering through a high-finesse Fabry–Perot etalon, which allows reaching a spectral resolution of ≈10 cm^{-1} (≈1.1 nm FWHM bandwidth), matching the linewidths of vibrational Lorentzian peaks [48]. The second replica, with ≈3-W average power, provides sufficient pulse energies (≈1.5 μJ) to generate a broadband near-infrared WLC by focusing it in a 10-mm-thick YAG crystal, which we employed as Stokes pulses. The broadband source shows very good stability with energy fluctuations <1% RMS comparable to those of the driving laser.

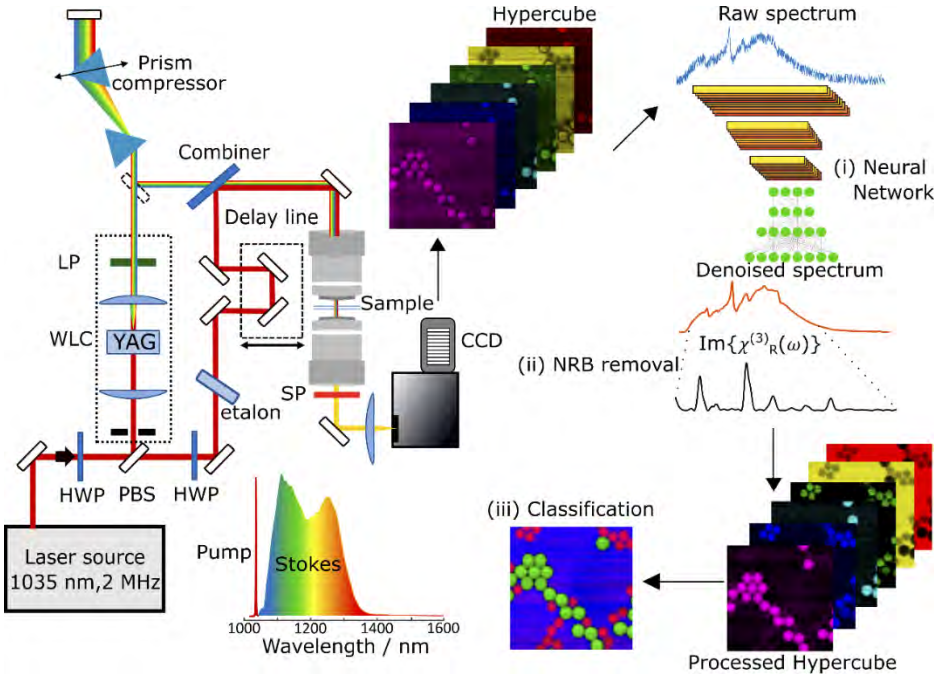

Fig. 1. Scheme of the B-CARS experimental setup. HWP: half-wave plate; PBS: polarizing beam splitter; LP: long-pass filter; SP: short-pass filter. Pump (red) and Stokes (rainbow) spectra. Schematic of the data processing pipeline: (i) Neural Network, (ii) NRB removal and (iii) Classification Methods to obtain false colors image.

Optics EXPRESS

A long-wave-pass filter selects the red-shifted lobe of the WLC (1050–1300 nm). The spectral energy density of the Stokes beam is high enough to generate CARS in the entire fingerprint region even at very short pixel-dwell times. An SF-11 prism pair compresses the Stokes pulse, compensating the dispersion introduced by the optical elements of the system. Before the microscope, the pump and Stokes pulses are collinearly superimposed through a dichroic mirror and temporally synchronized by a mechanical delay line. The beams are then sent to a homebuilt transmission microscope in up-right configuration equipped with two identical 100x air objectives with NA = 0.85. After the sample, a short-pass filter rejects the pump and Stokes beams, transmitting the generated B-CARS signal, whose spectrum is then measured with a standard grating-based dispersive spectrometer. The sample is raster-scanned in three dimensions using a motorized XYZ translation stage synchronized with the CCD camera of the spectrometer. Average powers of ≈40 mW for the pump and ≈10 mW for the Stokes beam have been used for all the experiments.

3. Results and discussion

3.1. B-CARS spectroscopy of solvents

To assess the performance of the system, we measured the spectral profiles of six solvents: acetone, ethanol, methanol, isopropanol, dimethyl sulfoxide (DMSO), and toluene (see Fig. 2(a)). For these experiments, using solvents droplets deposited between two 170-μm glass coverslips (see Fig. 2(b)), we set the CCD exposure time to 0.8 ms, i.e., the minimum allowed by the detector electronics, and collected single-point B-CARS spectra, spanning the whole fingerprint region from 500 to 2000cm^{-1}. The raw spectra (blue curves in Fig. 2(a)) show the characteristic distortions of the line shapes due to the interference of the resonant CARS signal with the NRB.

The single-point spectra retrieved applying the Kramers-Kronig algorithm [17] to remove the NRB contribution (red curves in Fig. 2(a)) show a very good agreement with the SR spectra (grey areas in Fig. 2(a)) both in the relative positions of the peaks and their amplitude ratios. We also examined the detection limit of our system measuring B-CARS spectra of a set of binary solutions of DMSO and pure water with variable DMSO concentration, ranging from 100% to 0%. We set the exposure time to 10-ms, averaging over a hundred spectra for a total of 1-second measurement time, and used the same sample configuration employed for solvents, i.e. the binary solution of DMSO and water at different dilutions between two glass coverslips. We did not apply any denoising method to the spectra, but we just retrieved the pure vibrational response of the solvents using the Kramers-Kronig algorithm to remove the NRB. As reference spectrum for the Kramers-Kronig algorithm, we used the CARS spectrum collected on the sample with pure water (0% DMSO – 100% water). The response of the retrieved Im$\{\chi_R{}^{(3)}\}$ is linear with respect to DMSO concentration (Fig. 2(c)) and we found that the detection limit of the system is ≈14.1 mmol/L. This limit corresponds to the value of the solvent concentration at which the main peak of DMSO in the fingerprint region at ≈667 cm^{-1} is equal to the background signal due to noise. The determined sensitivity limit corresponds to a two-fold increase with respect to previously reported multiplex CARS in the fingerprint region [14].

We then moved to imaging applications, collecting spectral hypercubes consisting of a B-CARS spectrum for each pixel of the image. B-CARS imaging is performed by raster scanning the sample in the x-y directions, keeping it fixed in the z axis, and simultaneously acquiring a CARS spectrum with the CCD. To extract the maximum amount of information from the high-speed measured B-CARS spectra, we designed a data post-processing pipeline, which is schematically shown in the right-hand part of Fig. 1. It consists of three steps: a CNN to remove the noise; the Kramers-Kronig algorithm [17] to extract the imaginary part of the resonant vibrational susceptibility, $Im[\chi_R^{(3)}(\omega)]$, followed by signal unmixing/clustering to distinguish the various sample components.

Optics EXPRESS

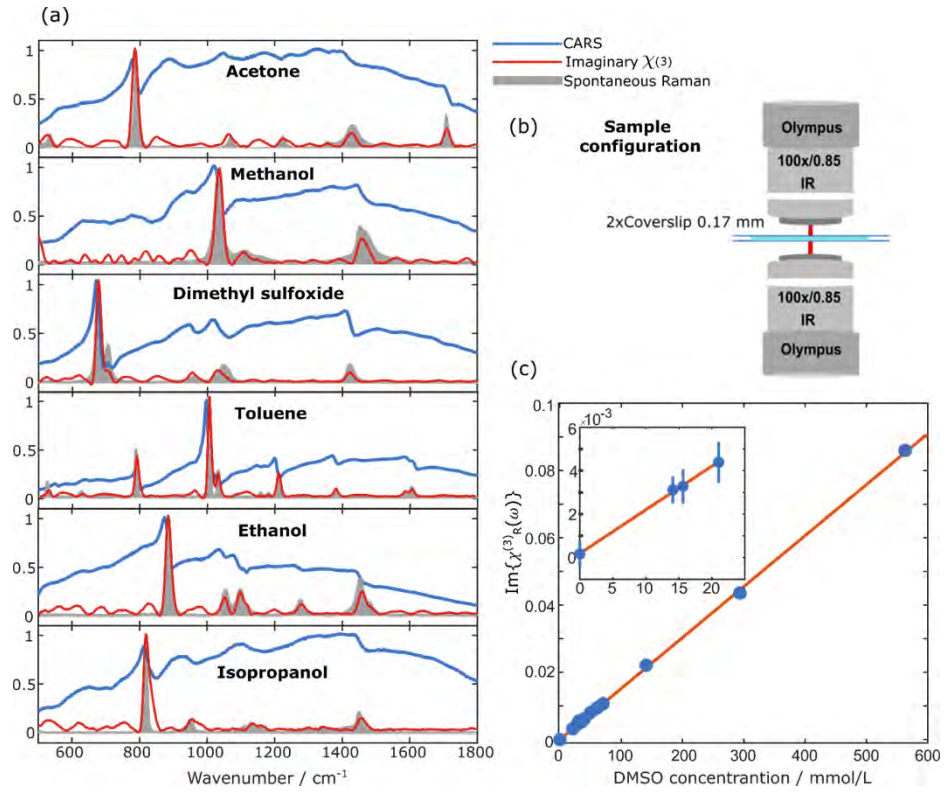

Fig. 2. (a) B-CARS raw single-point spectra (blue solid lines) measured at 0.8-ms exposure time on six solvents (as indicated), sandwiched between two 170-µm glass coverslips. Red solid lines are the corresponding imaginary parts of the nonlinear susceptibility, retrieved after applying denoising via deep learning and Kramers-Kronig algorithm. SR spectra (grey areas) are also plotted for comparison. (b) Scheme of the sample configuration employed for the experiments. (c) Dilution test experiment on a binary solution of DMSO and pure water. We considered the retrieved imaginary part of the third order resonant susceptibility of the main peak of DMSO at 667 cm^{-1}. The inset shows a zoom on the low concentration binary solutions. Estimated sensitivity: 14.1 mmol/L of DMSO in pure water. Error bars: 1 standard deviation.

The CNN used for spectral denoising (see Fig. 1) was inspired by the LeNet architecture [49] and is characterized by six convolutional layers, two average pooling layers and six fully connected layers. We chose a mean absolute percentage error loss function, a batch size of 128 training examples and a validation split of 20%, which proved to be best in terms of accuracy. The training dataset consists of high-SNR B-CARS spectra of six different spectroscopic grade solvents acquired with our system with long (100-ms) exposure time. The noisy inputs are obtained adding random noise with uniform distribution, while the outputs are obtained computing a moving average (3 points out of 1024) of the acquired spectra, which is enough to remove the random Gaussian noise but not the dispersive features. Then, we applied data augmentation [50] to the original dataset, reaching higher performances of the network during the training procedure.

We compared our denoiser with conventional algorithms (see Fig. 3(a)), namely the moving mean, the Fourier-transform filtering or the Savitzky-Golay filter. For the comparison, we used a B-CARS spectrum of toluene acquired at 100-ms exposure time and adding random noise uniformly distributed, that we first denoised on our trained CNN that had not previously seen

Optics EXPRESS

that specific spectrum. The moving mean returns a spectrum where each pixel is the local mean of k-point values, where each mean is calculated over a sliding window of length k across neighboring elements. The Fourier-transform approach operates a filter in the Fourier domain of the original spectrum, zeroing all the coefficients above a certain frequency, typically associated to noise, and then applies the inverse Fourier transform to obtain the denoised version of the spectrum. Finally, the Savitzky-Golay filter smooths the noisy spectrum fitting subsequent sub-sets of adjacent data points with a low-degree polynomial function using the method of linear least squares. These approaches show a lower prediction accuracy when compared to our denoising method via deep learning.

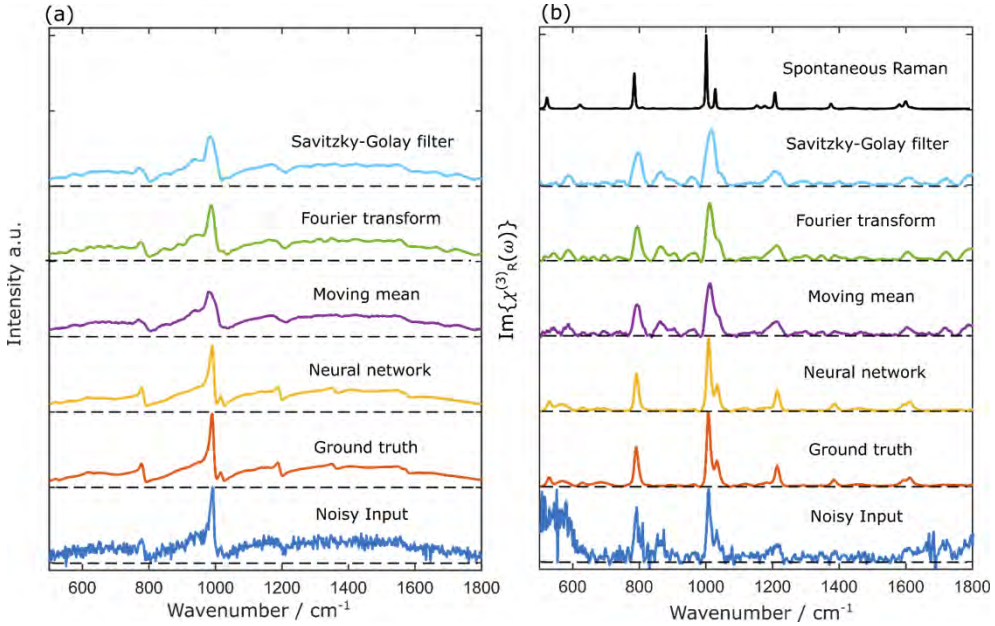

Fig. 3. Comparison of four different denoising methods on a CARS spectrum of toluene: Neural network, moving mean algorithm, Fourier-transform approach and Savitzky-Golay filter. (a) Denoising methods on a noisy input toluene CARS spectrum (blue curve) obtained considering experimental data and adding random noise. (b) $Im[\chi_R^{(3)}(\omega)]$ spectra retrieved through Kramers-Kronig algorithm starting from the spectra in panel (a). A SR spectrum (black curve) of toluene acquired with 5 s exposure time is reported for comparison.

The reason why classical mathematical methods are not suitable for this denoising task can be easily seen from the results in Fig. 3(a). Indeed, when considering CARS spectra, it is important to preserve the typical dispersive line shape given by the interference term between the resonant vibrational response of the sample and the NRB, which results in a slow rise, a steep decay, and another slow recovery of the signal with frequency. While our neural network can recognize and maintain original spectral features (see yellow curve), moving mean, Savitzky-Golay and Fourier-transform filtering approaches introduce artefacts and/or alter peak shapes. The moving mean with high k-values and Savitzky-Golay smooth the sharp edge of typical CARS peaks, whereas the Fourier transform cancels them by filtering out their typical high-frequency components. Eventually, we also applied the Kramers-Kronig algorithm to the different spectra (in Fig. 3(a)) to retrieve the imaginary part of the resonant third order susceptibility, $\chi^{(3)}$ (Fig. 3(b)). These results clearly demonstrate that our neural network outperforms conventional spectral denoising

Optics EXPRESS

methods. Further details on the model architecture, noise study of the model and the employed data augmentation methods are reported in the Supplementary Information.

3.2. B-CARS microscopy of a heterogeneous sample

Figure 4 shows images of a sample made by mixing 10-µm polystyrene (PS) and 8-µm polymethyl-methacrylate (PMMA) beads, immersed in DMSO. We collected single-pixel B-CARS spectra of PS, PMMA and DMSO at 1-ms integration time (panel 4(a)). In the spectral profiles, we highlighted, with black triangles, the three main peaks relative to the three chemical species (650 cm^{-1} for DMSO, 780 cm^{-1} for PMMA, 970 cm^{-1} for PS). Note that the positions of these peaks are shifted with respect to the corresponding ones in the SR spectra (grey areas in panel 4(c)) due to the distortions of the linewidths introduced by NRB. Panel 4(b) shows the portions of the hypercube we collected at these three specific vibrational frequencies. After our CNN-based spectral denoising and NRB removal, classification analysis was performed by applying the MCR-ALS algorithm [46], designed to retrieve the spectra and concentration maps of pure components from heterogeneous samples.

The hypercube **D**, obtained after denoising and NRB removal, can be written as the product of the concentration matrix **C** and of the spectra **S**, such that $\mathbf{D} = \mathbf{C}\mathbf{S}^{T}+\mathbf{E}$, where the superscript T stands for transpose, while **E** is a residual error that must be minimized by the algorithm. The number of components (i.e., the chemical species) in the algorithm can be arbitrarily selected. In our case, we fixed it to three. Panels 4(c)–(d) display the spectral profiles and the concentration maps obtained with the algorithm, without using any initial guess or prior knowledge on the spectra. The spectra are in very good agreement with the SR spectra (grey areas in panel 4(c)) and all the peaks, even the less intense ones, can be recognized. Note that in the retrieved spectrum of the 8-µm PMMA beads there is a residual peak of DMSO. This is caused by the fact that the sample thickness between the two coverslips is 10 µm, as set by the size of the PS beads, so that the DMSO solvent engulfs the smaller PMMA beads. This result confirms the capability of our B-CARS microscope of localizing and discriminating different chemical constituents in heterogeneous samples, working at high speed, and covering the entire fingerprint vibrational region.

3.3. Biological tissue imaging

Eventually, we used our B-CARS microscope for mapping biological specimens, imaging longitudinal sections of non-decalcified methyl methacrylate (MMA)-embedded murine spine (vertebrae). The 6-µm-thick sections include both the compact cortical part and the cancellous trabecular part of bone tissue, the latter being interspersed with bone marrow. Bone is constituted by a flexible matrix, mainly made up of type-I collagen, and by an inorganic mineral counterpart, mostly composed of calcium phosphate (hydroxyapatite), which gives rigidity to bones. The interplay of these two constituents provides tensile and compressive strength for load bearing. Conversely, bone marrow is rich in cells taking part in hematopoiesis, thus playing a crucial role for blood cell production. Consecutive tissue sections were deposited either on slides for routine histological procedures or on a poly-lysine treated quartz coverslip. After removing the resin, a second 170-µm quartz coverslip was applied to obtain a sandwich configuration. Further details on the sample preparation can be found in the supplemental document.

Figure 5(a) shows a bright-field image of a tissue slice stained with Hematoxylin and Eosin (H&E), typically used to visualize the sample morphology. From this image, we selected a reference 400×800-μm^2 field of view (dashed area) characterized by the presence of the cells of the bone marrow, the trabecular and cortical bone and the muscular tissue surrounding the vertebrae. We then imaged the unstained adjacent tissue slice by B-CARS in the same region. As a result, we acquired a hypercube and selected three frames (Fig. 5(b-d)) at three selected Raman shifts (i.e., 790 cm^{-1} for DNA, 960 cm^{-1} for hydroxyapatite and 1410 cm^{-1} for CH_2 of

Optics EXPRESS

proteins and lipids) corresponding to prominent peaks in CARS spectra (Fig. 5(e)). For the data processing, we adopted our CNN-based model for data denoising and the Kramers-Kronig algorithm for NRB removal. Then, we used KMCA to identify the main chemical constituents of the sample [47,51]. KMCA is preferred to MCR-ALS in this specific case, as we observed that it performs more effectively with a large sized dataset. Fixing the number of clusters to four, we obtained the concentration map and the spectra shown in Fig. 5(f-g). A cluster can be associated to the region of the vertebra related to cortical and trabecular bone, another one to the region associated to the bone marrow and the last one to the muscle (see Fig. 5(g)). The fourth cluster accounts for empty regions of the sample.

The centroid of the first cluster (in red) shows an intense band between 940 and 970 cm^{-1}, typically associated to phosphate bonds in hydroxyapatite (960 cm^{-1}). The spectrum also shows a small band around 1060-1080 cm^{-1}, representing carbonate in hydroxyapatite, and bands at 1220-1230 cm^{-1} (amide III, proteins), ≈1440 cm^{-1} (CH_2, proteins and lipids, also called organic matrix) and ≈1650 cm^{-1} (amide I, proteins) [52]. These spectral features clearly correspond to bone, mostly characterized by mineral crystals embedded in an organic protein-rich matrix. The centroids of the second and third clusters (in green and blue respectively) are mainly characterized

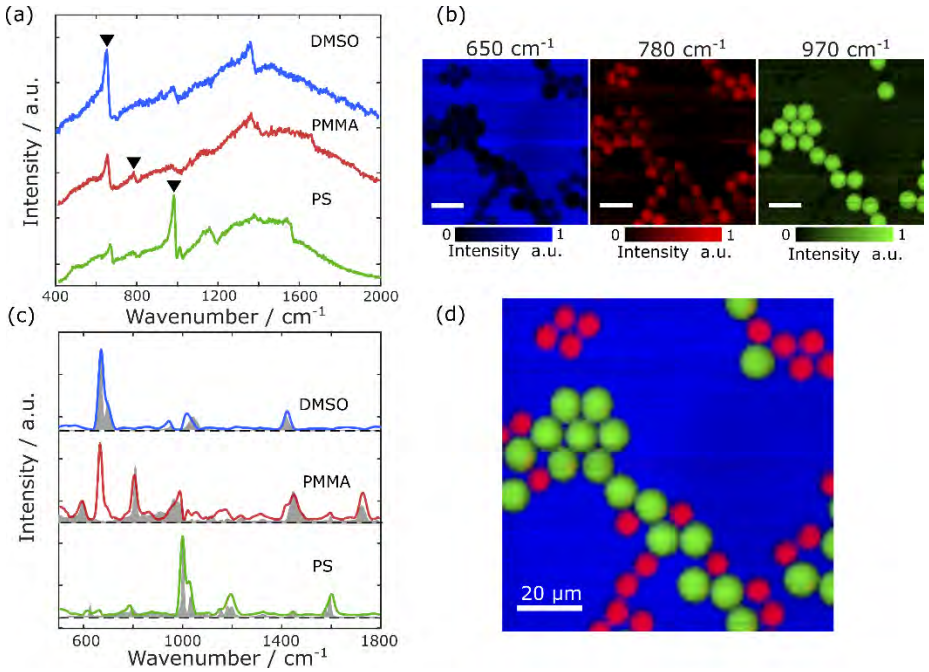

Fig. 4. Broadband CARS image of 10-µm PS and 8-µm PMMA beads soaked in DMSO and sandwiched between two 170-µm glass coverslips. (a) Single-pixel CARS spectra in the fingerprint region measured in correspondence with a PS bead (green curve), DMSO (blue curve) and a PMMA bead (red curve). (b) Frames of the measured B-CARS hypercube at three selected Raman shifts (black triangles in panel (a)) corresponding to three main characteristic peaks (650 cm^{-1} for DMSO, 780 cm^{-1} for PMMA, 970 cm^{-1} for PS) of the species in the fingerprint region. (c) MCR-ALS retrieved spectra of the three chemical species after the post-processing data pipeline and correspondent SR spectra (grey areas) (d) False-color image overlaying the three concentration maps retrieved with MCR-ALS analysis, with the same color code as (c). Imaging settings: 90×90 pixels, 1-µm pixel size, 1024 spectral points, 1-ms pixel dwell time, Scale bars: 20 µm, total image acquisition time: 8.1 s.

Optics EXPRESS

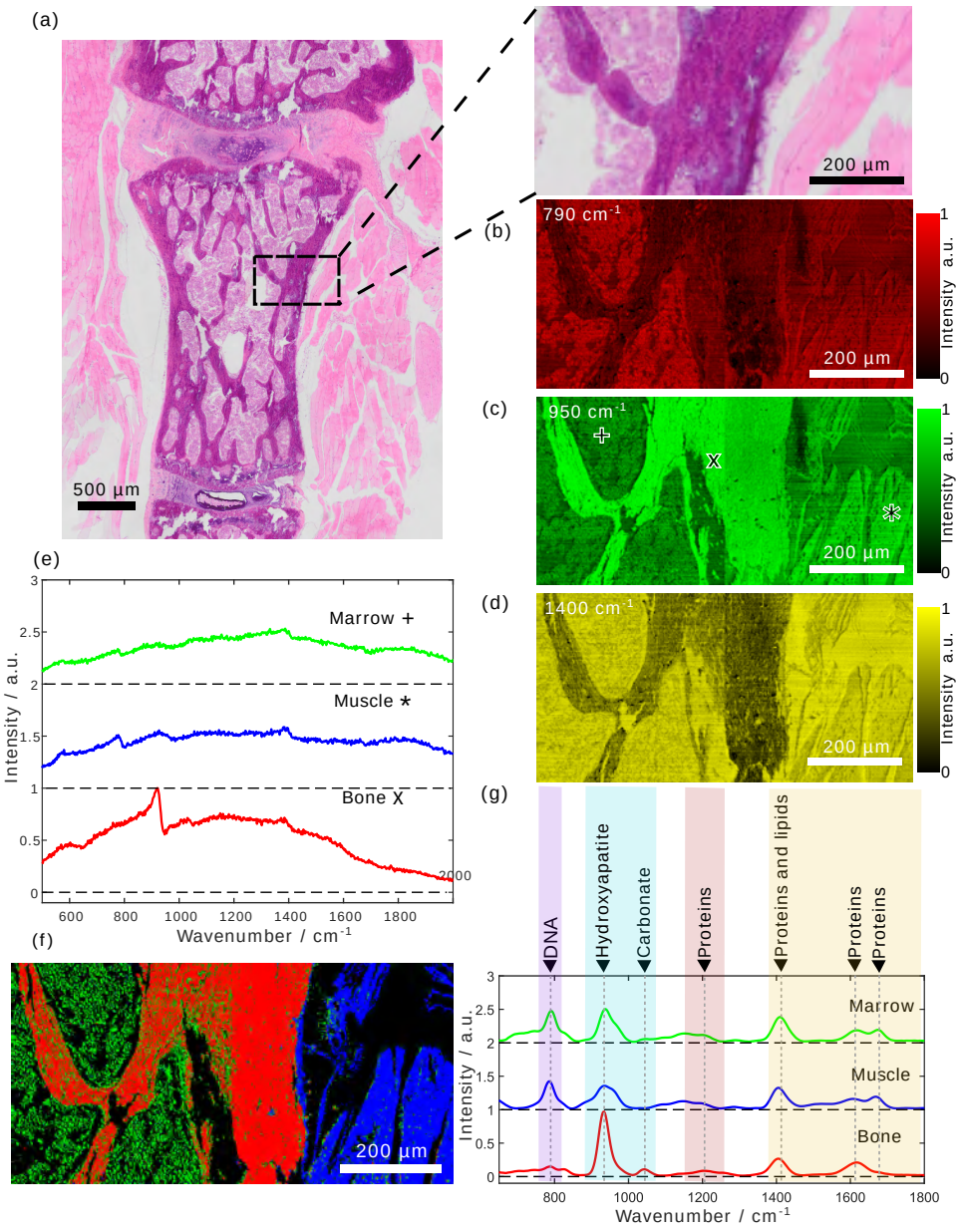

Fig. 5. Microscopy of 6-µm-thick murine spine sandwiched between two 170-µm quartz coverslips. (a) Bright-field image of a tissue slice stained with H&E. (b-d) Frames of the measured B-CARS hypercube at three different Raman shifts (black triangles in panel (e)) on the unstained adjacent slice. (e) B-CARS spectra from the bone marrow region (green curve, +), from the muscle region (blue curve, *) and from the bone tissue (red curve, x). (f-g) Concentration map and vibrational spectra of the three clusters associated with bone marrow, muscle, and bone, retrieved after denoising the data with the CNN model, NRB removal through the Kramers-Kronig algorithm and applying the KMCA algorithm. Imaging settings for the B-CARS dataset: 200-µm scale bar, 400×800 pixels, 1-µm pixel size, 1024 spectral points, 10-ms pixel dwell time, total image acquisition time: 55 minutes.

Optics EXPRESS

by vibrations around 790 cm^{-1}, typically assigned to DNA, and by strong signals in the spectral region between 1400 and 1700cm^{-1}, mainly associated to protein and lipids. These clusters can be assigned to bone marrow and to muscular tissue, characterized by a high cellular fraction and protein-rich muscle fibers, respectively.

3.4. Outlooks

We can envision significant improvements for our system. Preliminary measurements have shown that in a 10-mm YAG crystal it is possible to generate broader WLC (1050-1600 nm), allowing to also cover the CH-stretching region and detect the whole Raman spectrum of chemical analytes at 0.8-ms pixel dwell time. Figure S5 in the supplementary information reports an example of spectrum covering both fingerprint and CH-stretching region. However, the spectral distribution of this very broad WLC is not optimal, as most of the Stokes photons are in correspondence with the silent region of the vibrational spectrum and only their spectral tails are effectively employed for the fingerprint region on the one side and the C-H stretching region on the other. Therefore, it will be necessary to equalize the spectral distribution or even suppress the part of the Stokes spectrum associated to the silent region where no peaks are present, thus maximizing the SNR and reducing the unneeded optical power impinging on the sample. Moreover, owing to the high peak and average power of the driving laser, further developments of our B-CARS can be envisaged to shorten the pixel dwell time even more. These may include a line or wide-field illumination of the sample, thus retrieving the signal from an entire line or a two-dimensional field of view. For these applications, a higher average power both for the pump and Stokes beam can be used to illuminate the sample, without compromising its integrity. Indeed, light will be distributed on a larger area rather than on a single pixel, thus resulting in a comparable power density per pixel.

4. Conclusions

In this work we presented a novel configuration for high-speed label-free vibrational imaging, based on B-CARS spectroscopy. The two key novel elements introduced are: (1) the use of a low-repetition-rate (2 MHz) pulsed laser in the infrared and (2) the advanced data-processing pipeline, including an artificial intelligence algorithm for spectral denoising, phase retrieval and clusterization. The former innovation opens the possibility to: (i) Simplify the experimental setup, as the broadband Stokes light is not derived from tapered fibers or PCFs but rather by supercontinuum generation in bulk media, which is much more robust, compact, and insensitive to misalignments. (ii) Increase the nonlinear CARS signal, thanks to the higher pulse energy and peak power, for a given average power limited by sample damage, thus increasing the SNR and/or the imaging speed. (iii) Shift the wavelength of the pump/Stokes pulses beyond 1 µm, thus limiting the multi-photon sample damage when imaging biological samples. The second novelty, regarding the new post-processing algorithm, based on the combination of deep learning-based and conventional algorithms, was crucial to extract the relevant information from the measured hypercubes with a very large number of voxels, thus retrieving the same chemical information of conventional vibrational techniques, such as SR, but at the speed of CRS approaches.

Thanks to these innovations, we could demonstrate extremely fast (down to 0.8 ms pixel dwell time, limited by the CCD read-out time) B-CARS microscopy in the weak vibrational fingerprint region, with record-breaking sensitivity (down to 14.1 mmol/L) and high ($\approx$10 cm^{-1}) spectral resolution, without compromising sample integrity. We showed that the system could recognize the main chemical constituents in biological tissues such as longitudinal sections of murine vertebra in a label-free manner.

Our B-CARS approach will enable us to identify a wealth of biomolecules in heterogeneous media in a label-free manner, avoiding not only a cumbersome procedure for sample preparation but also the introduction of structural and chemical alterations to the sample that may lead to

Optics EXPRESS

artifacts during imaging and data processing. We envisage important applications in biomedical sciences, such as live cell imaging and histopathology.

Funding. European Commission (101016923); Regione Lombardia (POR FESR 2014-2020).

Acknowledgments. D.P. acknowledges funding from the European Union project CRIMSON under Grant Agreement No. 101016923 and from the Regione Lombardia project NEWMED under Grant Agreement No. POR FESR 2014-2020. F.V. thanks Francesco Crisafi for insightful discussions on the setup development.

Disclosures. The authors declare no conflicts of interest.

Data availability. Data underlying the results presented in this paper are available in Zenodo, see Ref. [53].

Supplemental document. See Supplement 1 for supporting content.

References

1. S. Pahlow, K. Weber, J. Popp, B. R. Wood, K. Kochan, A. Rüther, D. Perez-Guaita, P. Heraud, N. Stone, A. Dudgeon, B. Gardner, R. Reddy, D. Mayerich, and R. Bhargava, "Application of Vibrational Spectroscopy and Imaging to Point-of-Care Medicine: A Review," Appl. Spectrosc. **72**(1_suppl), 52–84 (2018).
2. R. Vanna, A. De la Cadena, B. Talone, C. Manzoni, M. Marangoni, D. Polli, and G. Cerullo, "Vibrational imaging for label-free cancer diagnosis and classification," Riv. Nuovo Cim. **45**(2), 107–187 (2022).
3. C. V. Raman and K. S. Krishnan, "A new type of secondary radiation [11]," Nature **121**(3048), 501–502 (1928).
4. R. Smith, K. L. Wright, and L. Ashton, "Raman spectroscopy: An evolving technique for live cell studies," Analyst **141**(12), 3590–3600 (2016).
5. C. Zhang and J. X. Cheng, "Perspective: Coherent Raman scattering microscopy, the future is bright," APL Photonics **3**(9), 090901 (2018).
6. C. L. Evans and X. S. Xie, "Coherent anti-Stokes Raman scattering microscopy: Chemical imaging for biology and medicine," Annu. Rev. Anal. Chem. **1**(1), 883–909 (2008).
7. D. Polli, V. Kumar, C. M. Valensise, M. Marangoni, and G. Cerullo, "Broadband Coherent Raman Scattering Microscopy," Laser Photonics Rev. **12**(9), 1800020 (2018).
8. J.X. Cheng, W. Min, Y. Ozeki, and D. Polli, *Stimulated Raman Scattering Microscopy: Techniques and Applications*, 1st Edition (Elsevier, 2021).
9. M. Hashimoto, T. Araki, and S. Kawata, "Molecular vibration imaging in the fingerprint region by use of coherent anti-Stokes Raman scattering microscopy with a collinear configuration," Opt. Lett. **25**(24), 1768 (2000).
10. A. Zumbusch, G. R. Holtom, and X. S. Xie, "Three-dimensional vibrational imaging by coherent anti-stokes raman scattering," Phys. Rev. Lett. **82**(20), 4142–4145 (1999).
11. A. De la Cadena, C. M. Valensise, M. Marangoni, G. Cerullo, and D. Polli, "Broadband stimulated Raman scattering microscopy with wavelength-scanning detection," J. Raman Spectrosc. **51**(10), 1951–1959 (2020).
12. A. De la Cadena, F. Vernuccio, A. Ragni, G. Sciortino, R. Vanna, C. Ferrante, N. Pediconi, C. Valensise, L. Genchi, S. P. Laptenok, A. Doni, M. Erreni, T. Scopigno, C. Liberale, G. Ferrari, M. Sampietro, G. Cerullo, and D. Polli, "Broadband stimulated Raman imaging based on multi-channel lock-in detection for spectral histopathology," APL Photonics **7**(7), 076104 (2022).
13. M. Müller and A. Zumbusch, "Coherent anti-Stokes Raman Scattering Microscopy," ChemPhysChem **8**(15), 2156–2170 (2007).
14. C. H. Camp, Y. J. Lee, J. M. Heddleston, C. M. Hartshorn, A. R. H. Walker, J. N. Rich, J. D. Lathia, and M. T. Cicerone, "High-speed coherent Raman fingerprint imaging of biological tissues," Nat. Photonics **8**(8), 627–634 (2014).
15. M. T. Cicerone, K. A. Aamer, Y. J. Lee, and E. Vartiainen, "Maximum entropy and time-domain Kramers-Kronig phase retrieval approaches are functionally equivalent for CARS microspectroscopy," in *Journal of Raman Spectroscopy* 43, 637–643(2012).
16. E. M. Vartiainen, "Phase retrieval approach for coherent anti-Stokes Raman scattering spectrum analysis," J. Opt. Soc. Am. B **9**(8), 1209–1214 (1992).
17. Y. Liu, Y. J. Lee, and M. T. Cicerone, "Broadband CARS spectral phase retrieval using a time-domain Kramers–Kronig transform," Opt. Lett. **34**(9), 1363–1365 (2009).
18. C. M. Valensise, A. Giuseppi, F. Vernuccio, A. De La Cadena, G. Cerullo, and D. Polli, "Removing non-resonant background from CARS spectra via deep learning," APL Photonics **5**(6), 061305 (2020).
19. R. Houhou, P. Barman, M. Schmitt, T. Meyer, J. Popp, and T. Bocklitz, "Deep learning as phase retrieval tool for CARS spectra," Opt. Express **28**(14), 21002–21024 (2020).
20. Z. Wang, K. O' Dwyer, R. Muddiman, T. Ward, C. H. Camp, and B. M. Hennelly, "VECTOR: Very deep convolutional autoencoders for non-resonant background removal in broadband coherent anti-Stokes Raman scattering," J. Raman Spectrosc. **53**(6), 1081–1093 (2022).
21. J. Y. Lee, S.-H. Kim, D. W. Moon, and E. S. Lee, "Three-color multiplex CARS for fast imaging and microspectroscopy in the entire CHn stretching vibrational region," Opt. Express **17**(25), 22281–22295 (2009).

Optics EXPRESS

22. F. Masia, A. Glen, P. Stephens, P. Borri, and W. Langbein, "Quantitative Chemical Imaging and Unsupervised Analysis Using Hyperspectral Coherent Anti-Stokes Raman Scattering Microscopy," Anal. Chem. **85**(22), 10820–10828 (2013).
23. E. R. Andresen, H. N. Paulsen, V. Birkedal, J. Thøgersen, and S. R. Keiding, "Broadband multiplex coherent anti-Stokes Raman scattering microscopy employing photonic-crystal fibers," J. Opt. Soc. Am. B **22**(9), 1934–1938 (2005).
24. M. Müller and J. M. Schins, "Imaging the thermodynamic state of lipid membranes with multiplex CARS microscopy," J. Phys. Chem. B **106**(14), 3715–3723 (2002).
25. H. Kano, T. Maruyama, J. Kano, Y. Oka, D. Kaneta, T. Guerenne, P. Leproux, V. Couderc, and M. Noguchi, "Ultra-multiplex CARS spectroscopic imaging with 1-millisecond pixel dwell time," OSA Continuum **2**(5), 1693–1705 (2019).
26. H. Yoneyama, K. Sudo, P. Leproux, V. Couderc, A. Inoko, and H. Kano, "Invited Article: CARS molecular fingerprinting using sub-100-ps microchip laser source with fiber amplifier," APL Photonics **3**(9), 092408 (2018).
27. K. Isobe, A. Suda, M. Tanaka, H. Hashimoto, F. Kannari, H. Kawano, H. Mizuno, A. Miyawaki, and K. Midorikawa, "Single-pulse coherent anti-Stokes Raman scattering microscopy employing an octave spanning pulse," Opt. Express **17**(14), 11259–11266 (2009).
28. W. Langbein, I. Rocha-Mendoza, and P. Borri, "Single source coherent anti-Stokes Raman microspectroscopy using spectral focusing," Appl. Phys. Lett. **95**(8), 081109 (2009).
29. T. W. Kee and M. T. Cicerone, "Simple approach to one-laser, broadband coherent anti-Stokes Raman scattering microscopy," Opt. Lett. **29**(23), 2701–2703 (2004).
30. J. Xu, B. Guo, K. K. Y. Wong, and K. K. Tsia, "Broadband hyperspectral coherent anti-Stokes Raman scattering microscopy for stain-free histological imaging with principal component analysis," Multiphoton Microscopy in the Biomedical Sciences XIV **8948**, 89480R (2014).
31. H. Kano and H. O. Hamaguchi, "Ultrabroadband (>2500 cm-1) multiplex coherent anti-Stokes Raman scattering microspectroscopy using a supercontinuum generated from a photonic crystal fiber," Appl. Phys. Lett. **86**(12), 121113 (2005).
32. M. Cui, M. Joffre, J. Skodack, and J. P. Ogilvie, "Interferometric Fourier transform Coherent anti-Stokes Raman Scattering," Opt. Express **14**(18), 8448–8458 (2006).
33. K. Hashimoto, M. Takahashi, T. Ideguchi, and K. Goda, "Broadband coherent Raman spectroscopy running at 24,000 spectra per second," Sci. Rep. **6**(1), 21036 (2016).
34. A. S. Duarte, C. Schnedermann, and P. Kukura, "Wide-Field Detected Fourier Transform CARS Microscopy," Sci. Rep. **6**(1), 37516 (2016).
35. T. Ideguchi, S. Holzner, B. Bernhardt, G. Guelachvili, N. Picqué, and T. W. Hänsch, "Coherent Raman spectro-imaging with laser frequency combs," Nature **502**(7471), 355–358 (2013).
36. C. S. Liao, J. H. Choi, D. Zhang, S. H. Chan, and J. X. Cheng, "Denoising Stimulated Raman Spectroscopic Images by Total Variation Minimization," J. Phys. Chem. C **119**(33), 19397–19403 (2015).
37. F. Vernuccio, A. Bresci, V. Cimini, A. Giuseppi, G. Cerullo, D. Polli, and C. M. Valensise, "Artificial Intelligence in Classical and Quantum Photonics," Laser Photon. Rev. **16**(5), 2100399 (2022).
38. B. Manifold, E. Thomas, A. T. Francis, A. H. Hill, and D. Fu, "Denoising of stimulated Raman scattering microscopy images via deep learning," Biomed. Opt. Express **10**(8), 3860–3874 (2019).
39. O. Ronneberger, P. Fischer, and T. Brox, "U-net: Convolutional networks for biomedical image segmentation," in *Lecture Notes in Computer Science* (Including Subseries Lecture Notes in Artificial Intelligence and Lecture Notes in Bioinformatics) 9351 (2015).
40. N. Yamato, H. Niioka, J. Miyake, and M. Hashimoto, "Improvement of nerve imaging speed with coherent anti-Stokes Raman scattering rigid endoscope using deep-learning noise reduction," Sci. Rep. **10**(1), 15212 (2020).
41. H. Lin, H. J. Lee, N. Tague, J. B. Lugagne, C. Zong, F. Deng, J. Shin, L. Tian, W. Wong, M. J. Dunlop, and J. X. Cheng, "Microsecond fingerprint stimulated Raman spectroscopic imaging by ultrafast tuning and spatial-spectral learning," Nat. Commun. **12**(1), 3052 (2021).
42. A.-L. Calendron, H. Çankaya, G. Cirmi, and F. X. Kärtner, "White-light generation with sub-ps pulses," Opt. Express **23**(11), 13866–13879 (2015).
43. A. Dubietis, G. Tamošauskas, R. Šuminas, V. Jukna, and A. Couairon, "Ultrafast supercontinuum generation in bulk condensed media," Lith. J. Phys. **57**(3), SG1–SG3 (2017).
44. B. Talone, M. Bazzarelli, A. Schirato, F. Dello Vicario, D. Viola, E. Jacchetti, M. Bregonzio, M. T. Raimondi, G. Cerullo, and D. Polli, "Phototoxicity induced in living HeLa cells by focused femtosecond laser pulses: a data-driven approach," Biomed. Opt. Express **12**(12), 7886 (2021).
45. Y. Fu, H. Wang, R. Shi, and J.-X. Cheng, "Characterization of photodamage in coherent anti-Stokes Raman scattering microscopy," Opt. Express **14**(9), 3942–3951 (2006).
46. I. Chitra Ragupathy, V. Schweikhard, and A. Zumbusch, "Multivariate analysis of hyperspectral stimulated Raman scattering microscopy images," J. Raman Spectrosc. **52**(9), 1630–1642 (2021).
47. Y. J. Liu, M. Kyne, C. Wang, and X. Y. Yu, "Data mining in Raman imaging in a cellular biological system," Comput. Struct. Biotechnol. J. **18**, 2920–2930 (2020).

Optics EXPRESS

48. J. X. Cheng, A. Volkmer, L. D. Book, and X. S. Xie, "An Epi-Detected Coherent Anti-Stokes Raman Scattering (E-CARS) Microscope with High Spectral Resolution and High Sensitivity," J. Phys. Chem. B **105**(7), 1277–1280 (2001).
49. Y. Lecun, L. Bottou, Y. Bengio, and P. Ha, "LeNet," Proc. IEEE (1998).
50. A. Bresci, M. Guizzardi, C. M. Valensise, F. Marangi, F. Scotognella, G. Cerullo, and D. Polli, "Removal of cross-phase modulation artifacts in ultrafast pump–probe dynamics by deep learning," APL Photonics **6**(7), 076104 (2021).
51. M. Miljković, T. Chernenko, M. J. Romeo, B. Bird, C. Matthäus, and M. Diem, "Label-free imaging of human cells: Algorithms for image reconstruction of Raman hyperspectral datasets," Analyst **135**(8), 2002–2013 (2010).
52. M. Unal, R. Ahmed, A. Mahadevan-Jansen, and J. S. Nyman, "Compositional assessment of bone by Raman spectroscopy," Analyst **146**(24), 7464–7490 (2021).
53. F. Vernuccio, A. Bresci, B. Talone, A. De la Cadena Perez-Gallardo, C. Ceconello, S. Mantero, C. Sobacchi, R. Vanna, G. Cerullo, and D. Polli, "Fingerprint multiplex CARS at high speed based on supercontinuum generation in bulk media and deep learning spectral denoising,"Zenodo2022https://doi.org/10.5281/zenodo.6772179